Boosting performances of ZnO microwire homojunction ultraviolet self-powered photodetector by coupled interfacial engineering and plasmonic effects

Kai Tang, Shulin Sha, Peng Wan, Yalin Zhai, Caixia Kan, Daning Shi[*] and Mingming Jiang[*]

ABSTRACT A highly sensitive self-biased ultraviolet (UV) photodetector is largely desirable in practical applications. This work develops a one-dimensional ZnO homojunction photodiode, which includes an Sb-doped ZnO microwire with surface-covered by Ag nanowires (AgNWs@ZnO:Sb MW), a MgO buffer nanolayer, and a ZnO film. The photodiode is dramatically sensitive to UV light, with its photosensitive performances of a large on/off ratio of approximately 10^7, a maximum responsivity of 292.2 mA W^{-1}, a high specific detectivity of 6.9×10^{13} Jones, and a rapid response speed in microseconds (16.4/465.1 μs) under 365-nm light illumination *via* 10 μW cm^{-2} at 0 V bias. In particular, the highest external quantum efficiency approaching 99.3% is achieved. The modulation of the MgO nanofilm and surface-modified AgNWs on the improved photoresponse was carefully examined. Acting as a self-biased optical receiver, this photodiode was further integrated into a UV communication system that can transmit information in real time. Also, a 9×9 photodetector array based on the AgNWs@p-ZnO:Sb MW/i-MgO/n-ZnO homojunction exhibited a uniform distribution of light response and could be used as a workable photosensory to achieve good spatial resolution images. This work proposes a promising route for the design of high-performance UV photodetectors for realistic applications with low power consumption and large-scale construction.

Keywords: interface engineering, p-type ZnO:Sb microwire, self-powered photodetector, imaging sensor, UV optical communication, plasmonic effect

INTRODUCTION

Photodetection devices, which allow electromagnetic radiation to be directly converted into electrical current, have been a topic attracting widespread interest due to their ever-growing applications, such as optical communications, photoimaging, and sensing [1–12]. Compared with traditional photodetectors (PDs), the development of self-biased photodetection devices, which are operated without any additional power source, is highly significant considering the growing energy demand due to their much smaller energy consumption, higher energy conversion efficiency, miniaturized structure and dimension, low-cost, integration, and so forth [13–16]. Usually, the p-n junction is the widely adopted device structure and has been extensively employed to construct self-powered PDs due to its robust built-in electric field and wide depletion region [17–23]. However, it is revealed that this type of self-biased PD, especially for low-dimensional devices, still faces numerous interfacial issues, such as severe leakage current, complicated trapping states and interface defects, and nonrecombination loss.

Different interface-optimizing strategies have been proposed to improve the photosensitive properties of photodiode devices, such as the incorporation of an insulating layer, which serves as a passivating medium, or the insertion of a tunneling layer [24–28]. Nevertheless, their insulating behaviors have currently resulted in several issues in the development of high-performance photodiodes, such as light absorption, energy conversion efficiency, transport paths, and response speed of photo-generated charge carriers. These drawbacks seriously limit their photodetection properties, including response speed, detection sensitivity, and external quantum efficiency (EQE) [29–32]. Despite these advantages of insulator materials, the obtained photodetection capabilities are still lower than expected. Thus, alternative experimental schemes for the rational design and engineering of p-n junction optoelectronic devices should be further developed to achieve higher sensitivity, faster response speed, and higher energy conversion efficiency [25,28,33].

In this work, a one-dimensional UV photosensitive device was fabricated, which was composed of a Sb-doped ZnO microwire covered by Ag nanowires (AgNWs@ZnO:Sb MW) serving as the p-component, a MgO buffer layer, and a ZnO film as the n-component. The device was highly sensitive to UV light and can be operated in a self-powered manner. This photodiode exceeds most reported ZnO-based PD devices and other state-of-the-art PDs. Especially, the EQE value approaching the theoretical limit of 100% was obtained. These advantageous performances are ascribed to the interface engineering of the interfaced MgO layer and surface-modified AgNWs. This work is anticipated to promote the development of high-performance self-biased UV PD for down-to-earth applications such as communications, imaging, and sensing.

EXPERIMENTAL SECTION

Synthesis of ZnO:Sb MWs

Individual ZnO MWs doped with antimony (Sb) were success-

fully synthesized by catalyst-free chemical vapor deposition (CVD) [19,26]. Typically, powders of ZnO, Sb_2O_3, and graphite (all from ZhongNuo Advanced Material Technology Co., Ltd.) with a $ZnO:Sb_2O_3$:graphite weight ratio of 9:1:10 were finely ground by hand for approximately 3 h. Then, the precursor mixture was placed in a corundum boat and covered with a clean silicon (Si) chip. The boat was then positioned in the heating zone in a horizontal double-zone furnace. Before heating, the tube furnace was flushed with high-purity argon (Ar) gas at a constant flow rate of approximately 250 standard cubic centimeter per minute (sccm) to remove any residual oxygen (O_2) in the tube. The heating module was quickly heated to 1100°C using the temperature control program of the tube furnace. A steady flow of approximately 125 sccm Ar gas was continuously introduced into the tube during the heating process. The temperature was maintained at 1100°C for 1 h to complete the reaction of the precursor. Afterward, a flow of O_2 was flown into the furnace chamber (10 sccm) as a growth gas, and the reaction was continued for approximately 30 min. Upon completion of the reaction, the tube furnace was naturally cooled to indoor temperature. The ZnO:Sb MWs were collected individually around the Si chip and corundum boat.

The AgNWs sample was prepared using an improved polyol method [34]. Using spin-coating technology, AgNWs could be uniformly deposited on the surface of an individual ZnO:Sb MW, thus obtaining a hybrid structure of AgNWs@ZnO:Sb wire. The fabrication process is presented in the Supplementary information.

Device fabrication

A PD that can detect UV light was successfully fabricated [19,26]. The principal device architecture was composed of an individual AgNWs@p-ZnO:Sb MW, an MgO buffer nanolayer, and an n-type ZnO film substrate. First, an approximately 200 nm-thick ZnO film was epitaxially grown on a sapphire substrate using a molecular beam epitaxy (MBE) system equipped with Oxford radiofrequency (RF) atom sources. Subsequently, a 60 nm-thick Au Ohmic contact electrode was deposited on one side of the ZnO film via electron beam heating evaporation. In the third step, a 100 nm-thick MgO film was deposited on the opposing side of the ZnO film using electron beam evaporation. Subsequently, an ultrathin 10 nm-thick MgO film was additionally deposited on the blank ZnO film. Next, a single AgNWs@ZnO:Sb MW was positioned onto the MgO buffer layer through mechanical transfer. One segment of the wire was precisely aligned with the Au nanofilm situated on the MgO layer. Ultimately, an Au electrode was meticulously fabricated on the segment of the AgNWs@ZnO:Sb MW structure, which was precisely positioned atop the underlying Au nanofilm.

Materials and device characterizations

Scanning electron microscopy (SEM, TESCAN LAYRA3 GM) was used for the surface morphological characterization of AgNWs and ZnO:Sb MWs without and with AgNWs decoration. The crystal structures of the samples were characterized by X-ray diffraction (XRD, Malvern Panalytical, Empyrean). Optoelectronic property tests were conducted using a semiconductor device analyzer (Keysight, B1500A), equiped with a light source (Energetiq, EQ99X), and monochromator (Zolix, Omni-λ200i). The response speed of the fabricated device was assessed using a Nd:YAG pulsed laser (Ekspla, NT342) and a digital oscilloscope (Tektronix, MSO54). All these tests were performed under ambient conditions at the specified temperature.

RESULTS AND DISCUSSION

Briefly, the ZnO:Sb MWs were synthesized individually by catalyst-free CVD [19,26]. An optical photograph of the sample is exhibited in Fig. S1. The ZnO:Sb MW samples show a well-defined wire shape, and their lengths are measured on average to approximately 2.0 cm. Fig. 1a depicts an SEM image of ZnO:Sb MWs, which discloses that the samples are on average 15 μm in diameter. Therefore, the length/diameter ratio can reach approximately 1400. The samples display extremely smooth surfaces and square cross-sections, which implies that CVD-synthesized ZnO:Sb MWs have outstanding crystallization properties. The elemental composition of the ZnO:Sb wire was determined by energy-dispersive X-ray spectroscopy. The elements (Zn, O, and Sb) are uniformly distributed over the entire wire, as shown in Fig. 1b. The XRD pattern of the ZnO:Sb MWs in Fig. 1c presents three diffraction peaks at 31.71°, 34.41°, and 36.20°, which can be indexed to the (100), (002), and (101) planes of wurtzite ZnO, respectively.

AgNWs were synthesized using an optimized polyol method. The synthesis of AgNWs is presented in the Supplementary information [34]. The optical absorption spectrum of the as-synthesized AgNWs is plotted in Fig. S2. The absorption peak at 370 nm arises from a localized plasmonic effect [14–16]. A hybrid structure based on a ZnO:Sb MW with surface-modified AgNWs was constructed by spin-coating. The fabrication process is described in the Supplementary information (Fig. S3). The AgNWs-modified ZnO:Sb MW is imaged in the inset of Fig. 1d. The optical absorption properties of the ZnO:Sb MWs with and without AgNWs were measured. As shown in Fig. 1d, the surface-modified AgNWs can improve the optical absorption in the UV wavelengths, due to the UV plasmons of surface-covered AgNWs [33]. Further theoretical analysis is presented in Fig. S4 [14].

The effect of AgNWs on the photoelectric properties of a ZnO:Sb MW was examined. Using Au as the metal electrodes, an individual ZnO:Sb MW uncovered or covered with AgNWs was used to construct metal-semiconductor-metal (MSM) structure devices. As shown in Fig. 1e, the current-voltage (I-V) characteristics of the devices were measured in the dark and under 365-nm light irradiation. An individual AgNWs@ZnO:Sb MW MSM device is schematically shown in the inset of Fig. 1e. The I-V curves plotted in darkness exhibit approximatively linear characters, which implies that Au electrodes can make good Ohmic contact with ZnO:Sb MW regardless of whether they are uncovered or covered with AgNWs. As the devices were illuminated at 365 nm, electronic transport properties underwent significant changes. By comparison, the ZnO:Sb MW, which is modified using AgNWs, has a higher photocurrent. Further testing of the MSM devices upon 365-nm light illumination at 2 V bias was conducted for current-time (I-t) curves (light power density of 9.4 mW cm^{-2}). As illustrated in Fig. 1f, the photocurrent of AgNWs@ZnO:Sb MW MSM rapidly increases to 2.03 mA when the light source is turned on. When the light source is turned off, it returns to a dark current of approximately 1.53 mA. By comparison with the unmodified MSM device, the obtained photocurrent is increased by a factor of 50-fold. The
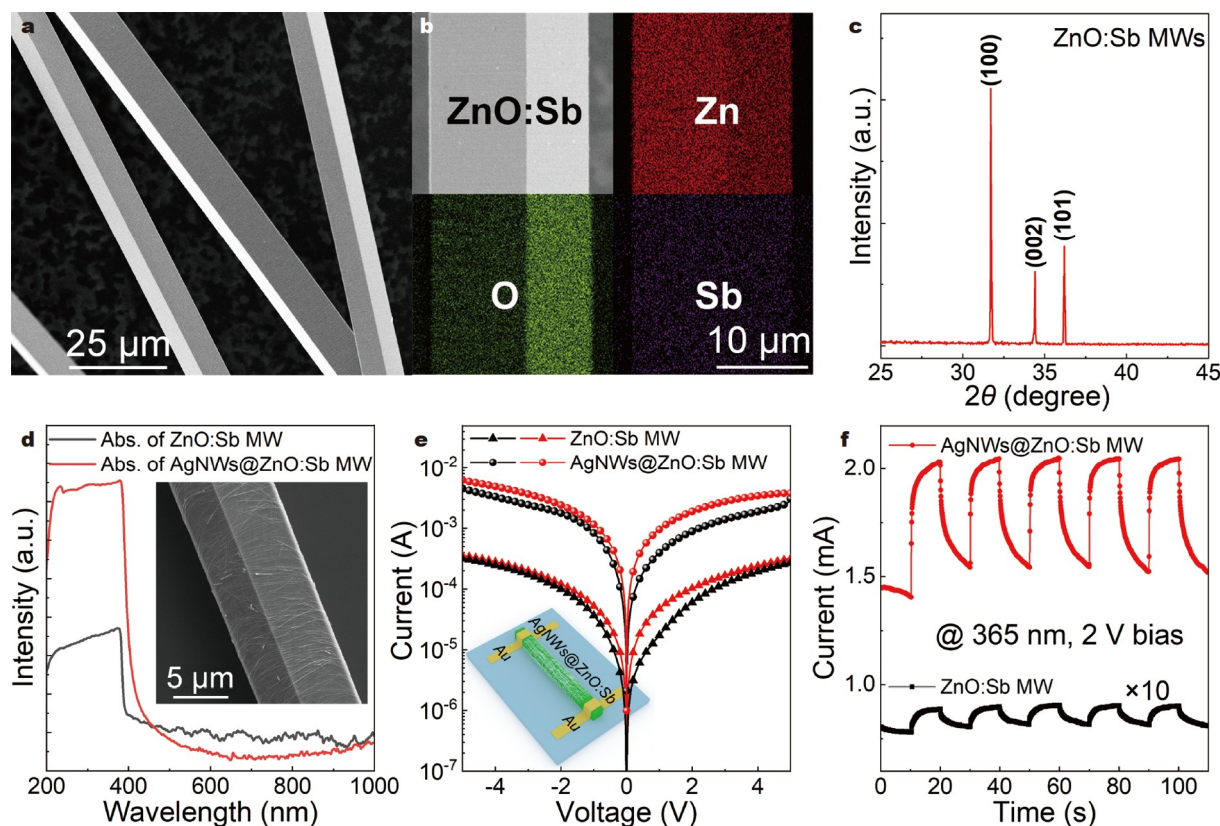
Figure 1 Characterization of CVD-prepared ZnO:Sb MWs. (a) SEM of individual ZnO:Sb MWs. (b) Elemental constituents of a ZnO:Sb MW. (c) XRD analysis of ZnO:Sb MWs. (d) Absorption spectra of ZnO:Sb MWs without and with AgNWs deposition. Inset: SEM of an AgNWs@ZnO:Sb MW. (e) *I-V* curves of a ZnO:Sb MW without and with AgNWs deposition when measured in darkness and under 365-nm illumination. The inset is a schematic architecture of the AgNWs@ZnO:Sb MW MSM structure device, where Au is the metal electrodes. (f) *I-t* curves of a ZnO:Sb MW with and without AgNWs deposition. During the measurements, the devices were illuminated by a 365-nm light source.

significant improvement in the photocurrent discloses that AgNWs can effectively change the near-field and improve the light absorption of a single MW by excitation of localized surface plasmon resonances, leading to higher photoelectric conversion efficiency under UV light [15,33,35].

Field-effect transistors (FETs) were fabricated to experimentally explore the electrical features of a single ZnO:Sb wire [36,37], with the n^{++}-doped Si used as the gate electrode for the back-gate FET structure. In addition, a 250 nm-thick SiO_2 was deposited on the heavily doped Si substrate. An individual ZnO:Sb MW was placed on the SiO_2/Si substrate, with Au films serving as the metal electrodes. A three-terminal FET architecture based on a single ZnO:Sb MW is illustrated in the inset of Fig. 2a, where Au acts as the source and drain electrodes. As shown in Fig. 2a, the curves of source-drain current (I_{ds}) *versus* source-drain voltage (V_{ds}) at different back-gate voltages (V_g) display standard linear behavior, suggesting that the contact between the Au metal electrodes and the CVD-synthesized ZnO:Sb MW is Ohmic contact. High-magnification observations of the I_{ds}-V_{ds} curves at around 1.0 V are further illustrated in Fig. 2b. Clearly, the changes in I_{ds}-V_{ds} character highly depend on V_g. Fig. 2c shows the gate-sweep characteristics of a ZnO:Sb MW at $V_{ds} = 1.0$ V. With increasing negative gate bias, the monotonic increase behavior of the I_{ds} definitively verifies the p-type conductivity of the CVD-synthesized ZnO:Sb wires [37,38].

As the ZnO:Sb MW FET device was modified using AgNWs, electrical measurements were further performed. Accordingly,

the characteristic curves of I_{ds}-V_{ds} with respect to different V_g values are shown in Fig. 2d, e. Besides the established linear correlation and the V_g-dependent behavior, a discernible enhancement in the electronic properties of the individual ZnO:Sb MW was achieved. The linearly increasing dependence between I_{ds} and V_g is shown in Fig. 2f. Conclusively, with surface-modified AgNWs, the transport properties of ZnO:Sb MW can be modulated. The effect of AgNWs on the transport parameters of a ZnO:Sb MW was rigorously examined and quantitatively evaluated. Parameters such as electrical conductivity, charge carrier mobility, and carrier concentration were calculated. Details of the calculation are presented in Supplementary information. Consequently, the electrical characteristics of a ZnO:Sb MW with and without AgNWs decoration can be quantitatively assessed (Table 1). Thus, the electrical properties of low-dimensional semiconductors, especially their mobilities, can be dramatically improved by cladding metal nanostructures [14,15,35].

Using AgNWs@ZnO:Sb MW as the predominant photo-absorber, a p-i-n homostructure photodetection device that integrates a MgO buffer layer and n-ZnO planar substrate was developed and constructed [19,26]. A schematic of the as-designed AgNWs@p-ZnO:Sb MW/i-MgO/n-ZnO homostructure photodiode is illustrated in Fig. 3a. The photoelectric properties of the as-prepared device were examined. Fig. 3b shows the *I-V* curves of the device in the dark. The ideality factor, as per the thermionic emission model, is assessed to be
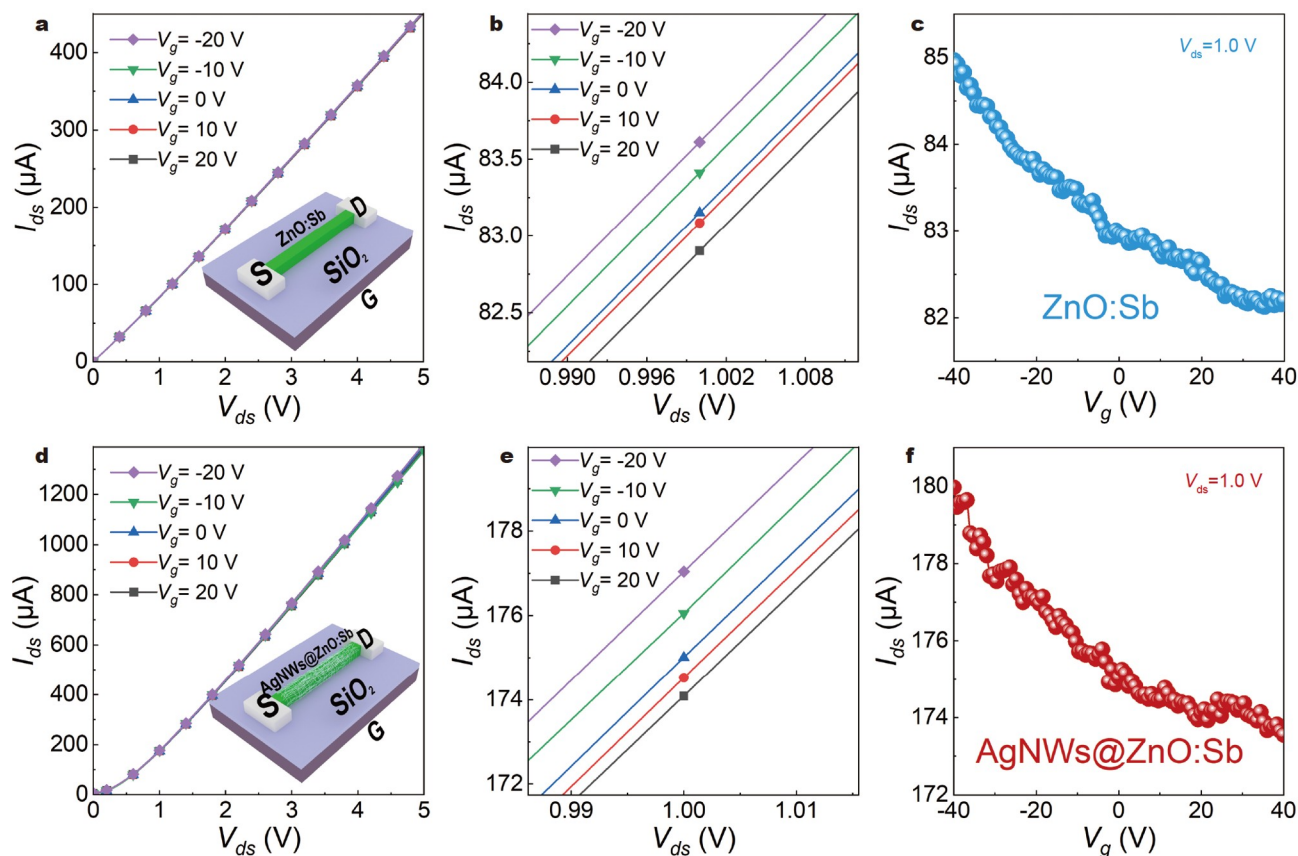
Figure 2 Transport measurements of a single ZnO:Sb wire uncovered and covered with AgNWs. (a) Dependence of I_{ds}-V_{ds} curves on various back-gate voltages V_g of a ZnO:Sb MW-based FET device. The inset is a schematic of the ZnO:Sb MW-based FET device. (b) Magnified area of I_{ds}-V_{ds} at different V_g around 1.0 V. (c) Change in I_{ds} *versus* V_g when calculated at V_{ds} = 1.0 V. As the single ZnO:Sb MW-based FET was modified using AgNWs, (d) the I_{ds}-V_{ds} curves are plotted at different V_g values. The inset is a schematic architecture of the AgNWs@ZnO:Sb MW-based FET. (e) Magnified area of I_{ds}-V_{ds} plotted at different V_g around 1.0 V. (f) Change in I_{ds} with different V_g when plotted at V_{ds} = 1.0 V.

Table 1 Electrical properties of a ZnO:Sb MW without and with AgNWs decoration

Parameters	ZnO:Sb	AgNWs@ZnO:Sb
Diameter (µm)	12	12
Channel length (µm)	100	100
Mobility (cm^2 V^{-1} s^{-1})	42.1	88.2
Conductivity (S cm^{-1})	0.1	0.2
Carrier density (cm^{-3})	1.25×10^{17}	1.26×10^{17}

approximately 0.99 when the forward bias is in the range of 0.03–0.12 V [39]. The device displays good rectifying behavior at ±2 V bias (rectifying ratio about 1.2×10^6). The zero-bias dark current is determined to be approximately 10^{-12} A. To elucidate the spectral responsivity of the fabricated device, the photoresponse characteristics were studied under different wavelengths of incoming light. Fig. 3c shows the photocurrent curves in the dark and upon light irradiation at different wavelengths of 300, 355, 365, and 375 nm. The I-V characteristics show substantial disparities between the dark current and the photocurrent. There is a substantial increase in the short-circuit current (I_{sc}) as the light wavelengths range from 300 to 365 nm. The device records the strongest I_{sc} when illuminated under 365-nm light. As the light wavelengths increased up to 375 nm, the I_{sc} decreased appropriately. This demonstrates that the as-prepared device has remarkable photovoltaic properties in the UV band.

An in-depth investigation of the relationship between wavelengths and photoresponse was performed, and the results are shown in Fig. 3d. An outstanding photoresponse property is shown when the wavelength falls below 365 nm. The photocurrent reaches the largest value of approximately 100 nA at a wavelength of 365 nm (maintaining a constant power of 80 µW cm^{-2}) [40]. It precisely indicates that the strongest response peak of this device occurs at 365 nm (marked in purple). Moreover, the UV/visible rejection ratio ($I_{365\ nm}/I_{400\ nm}$) is as high as five orders of magnitude, demonstrating that the as-constructed AgNWs@p-ZnO:Sb MW/i-MgO/n-ZnO homojunction photodiode has outstanding detecting capacity under 365-nm light illumination. To systematically evaluate the photodetection ability of the as-constructed PD, photoelectric performances were assessed. Under 365-nm light source irradiation with a range of light intensities P from 0.01 to 0.63 mW cm^{-2}, the device shows outstanding photovoltaic properties. For instance, the open-circuit voltage (V_{oc}) varies from 0.45 to 0.98 V, as shown in Fig. 3e. Similarly, I_{sc} is as high as 10^{-5} A in the photoresponse measurement. Therefore, the as-constructed AgNWs@p-ZnO:Sb MW/i-MgO/n-ZnO homojunction device
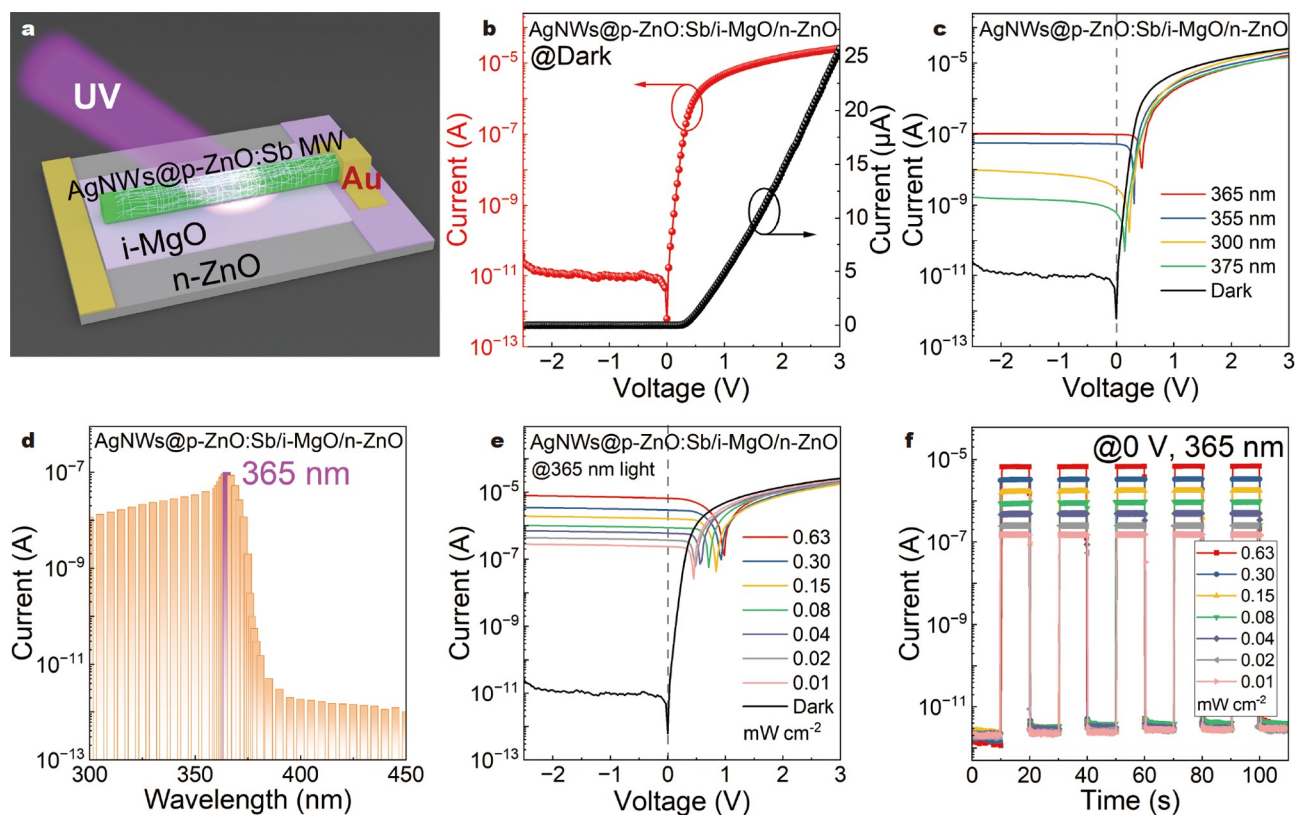
Figure 3 Characterizations of the as-prepared AgNWs@p-ZnO:Sb MW/i-MgO/n-ZnO homostructure device for UV detection. (a) Schematic architecture of the detector. (b) I-V curves plotted in the dark. (c) Logarithmic I-V characteristic curves of the device when tested in the dark and under 300-, 355-, 365-, and 375-nm light illumination. (d) Wavelength-dependent photocurrents of the device when tested in a self-biasing manner. (e) Logarithmic I-V characteristics of the device in the dark and upon 365-nm light irradiation with different power densities. (f) I-t curves of the PD obtained from on-off switching tests under different intensities of 365-nm light.

can operate in a self-biasing manner [6,15,41]. Illumination light density-dependent photoswitching performance is presented in Fig. 3f. The photocurrent response depicts a pronounced correlation with the on/off modulation of the UV light. Also, with the increase in light intensity, a substantial increase in I_{sc} is observed. The I_{sc} values under illumination remain stable after five cycles. Therefore, our constructed photodiode has a clear and rapid response when switching the light source.

The relationship between photocurrent I_{ph} ($I_{ph} = I_{light} - I_{dark}$) and 365-nm illumination was examined. Fig. 4a plots the fitted curve, which describes the dependence of I_{ph} on the incoming light intensity. In general, the relationship between I_{ph} and P follows the power law $I_{ph} = AP^{\theta}$ [36]. By fitting the curve, $\theta \sim 0.94$, which is close to that of low trapping states junctions ($\theta \sim 1$). That is, there are very few trapping states and complex processes in the as-fabricated photodiodes [42]. The detection characteristics for without and with the MgO buffer layer are further elucidated in Figs S5 and S6, respectively. Fig. 4b reveals the light intensity-dependent on-off ratio I_{on}/I_{off} of the device. The dark current at zero bias is evaluated to about 10^{-12} A. As the device is illuminated using a 365-nm light source via 0.63 mW cm^{-2}, the I_{on}/I_{off} is about 1.1×10^{5}. By incrementally increasing the P of the 365-nm light source to a level of 0.63 mW cm^{-2}, the I_{on}/I_{off} can reach 4.9×10^{6}.

Two key photodetection metrics, namely, responsivity (R) and specific detectivity (D^*), of the as-constructed photodiode were assessed. Generally, R is defined as

$$R = \frac{I_{ph} - I_d}{PS}, \tag{1}$$

where P and S are the illumination power density and active illuminated area, respectively. D^*, which characterizes the sensitivity of a PD device in detecting low-level optical signals, is calculated using [23]

$$D^* = \frac{R}{\sqrt{2eJ_d}}, \tag{2}$$

where R, e, and J_d are the responsivity, elementary charge, and dark current density, respectively. Fig. 4c presents the wavelength-dependent R and D^* of the as-prepared detector device in self-powered mode. The largest R of 225.0 mA W^{-1} is located around 365 nm. The UV/visible rejection ratio ($R_{365\,nm}/R_{400\,nm}$) is estimated to be approximately 10^5, which demonstrates that the as-proposed photodetecting device displays outstanding spectrally selective properties in the UV region. On the other hand, the maximum value D^* (5.8×10^{13} Jones) is similarly centered at 365 nm. The light power-dependent R and D^* are depicted in Fig. 4d. The largest R and D^* reach up to 292.2 mA W^{-1} and 6.9×10^{13} Jones at a low power of light intensity via 10 μW cm^{-2}, respectively. With increasing light intensity, the R and D^* values show a nonlinear decreasing trend but are still kept at a higher order of magnitude even at high light intensity [42–44]. Moreover, R and D^* reveal a clear decrease with increasing optical power density of incoming light, which results from the improved recombination activity of photogenerated electron-
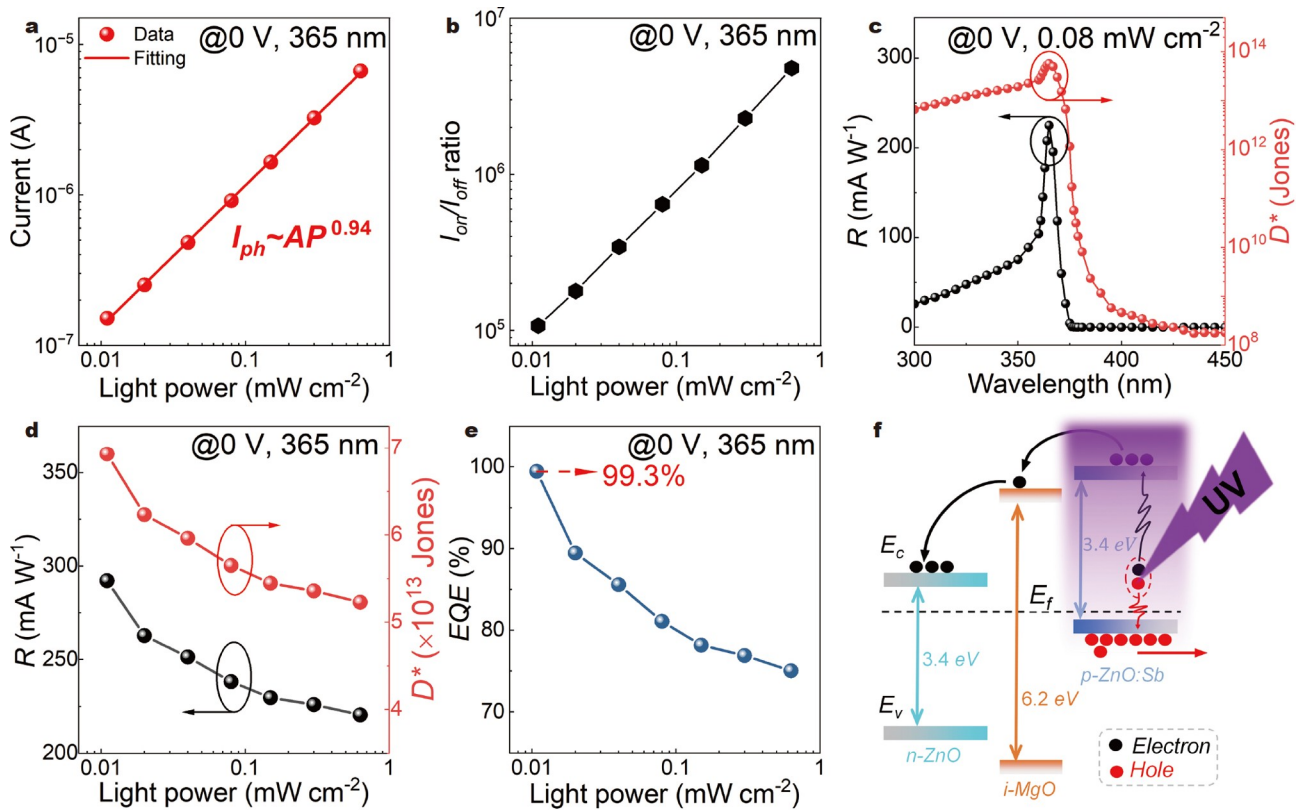
Figure 4 Device characterizations and working mechanism. (a) Light intensity-dependent photocurrents of the device when measured at a bias of 0 V. (b) Light intensity-dependent I_{on}/I_{off} of the device when measured at a bias of 0 V. (c) Wavelength-dependent R and D^*. (d) Variations of R and D^* with different intensities of 365-nm light. (e) Change in EQE of the device with different power intensities of 365-nm light. (f) Schematic representation of the energy-band diagram of the device depicted at 0 V bias under 365-nm UV light illumination.

holes at a higher level of illumination light densities.

As a key figure-of-merit of the PD device, EQE, which describes the specific value between the number of photo-induced electron holes dedicated to the detected photocurrent and the number of incoming photons, was considered. It evaluates the photoelectric conversion efficiency using [45]

$$EQE = R \times \frac{hc}{e\lambda}, \tag{3}$$

where h, c, and λ are the Planck constant, light velocity, and incident light wavelength, respectively. At a low power density of 10 μW cm^{-2}, the highest EQE approaching 99.3% is obtained, as exhibited in Fig. 4e. As the light intensity varies from 0.01 to 0.63 mW cm^{-2}, the EQE keeps a value larger than 75%. These phenomena collectively show that the combination of an MgO buffer layer and AgNWs can effectively realize proper interface optimization, thus giving an alternative scheme for improving device performance, especially for photoelectric conversion efficiency.

The working mechanism can be elucidated using the energy-band diagram in Fig. 4f. The theoretical distribution width of depletion in the p-ZnO:Sb region ($w_{ZnO:Sb}$) and n-ZnO region (w_{ZnO}) were assessed [36]. The corresponding $w_{ZnO:Sb}$ and w_{ZnO} are calculated to be approximately 76.5 and 0.7 nm, respectively. Details of the calculation are shown in the Supplementary information. Under UV light illumination, incoming photons with energies larger than 3.37 eV are mostly absorbed by the top ZnO:Sb MW. The absorbed photons would excite ZnO:Sb MW to produce abundant electron-hole pairs. With a rational design,

the as-prepared detector device shows the desired unipolar barrier characteristics, i.e., a large valence-band offset (ΔE_v) and a negligible conduction-band offset (ΔE_c) across the ZnO:Sb/MgO interface. Carrier transport behaviors were carefully modulated by the energy-band structure. The photogenerated electrons would undergo a small potential barrier in the conduction band of n-ZnO, which is driven by the built-in electric field. Meanwhile, the large ΔE_v at the ZnO:Sb/MgO interface can effectively block the photogenerated holes traveling from the ZnO:Sb MW to the underlying ZnO. Interface recombination and nonrecombination loss can be effectively suppressed at the ZnO:Sb/ZnO interface [19,46]. Thus, the carrier recombination centers could be efficiently reduced, thus facilitating the separation and transport of photocarriers.

For PDs used in optical communication, imaging, and similar fields, the response speed is a critical figure of merit. In Fig. 5a, a single-period I-t curve of the as-prepared detector device at 0 V bias is presented (taken from Fig. 3f). Both the rise time τ_r and decay time τ_d are calculated to be smaller than 0.5 s, which are limited by the measurement equipment. To accurately evaluate the response time, the photoresponse of the device exposed to pulsed laser signals was studied [36]. Fig. 5b exhibits the transient photoresponse of the as-prepared detector device under 365-nm pulse laser irradiation. The test system is described in the Supplementary information (Fig. S7). From Fig. 5c, a τ_r of about 16.4 μs and a τ_d of about 465.1 μs can be estimated, respectively [5,19]. The response times of devices without/with the MgO in-between layer, without and with surface-covered
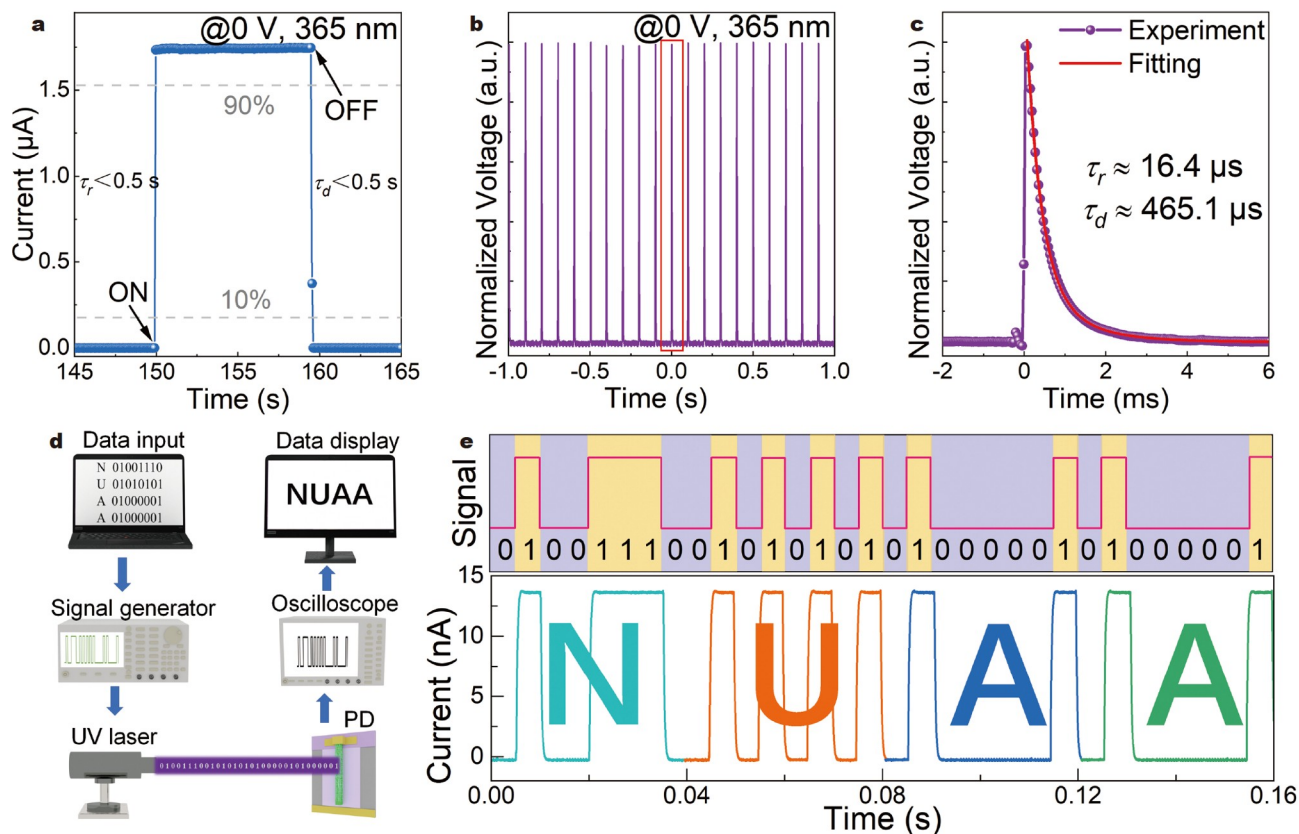
Figure 5 UV light communication system tests. (a) *I-t* curve of the as-prepared detector device under 365-nm irradiation. (b) Transient photoresponse of the device under 365-nm pulse laser illumination. (c) Single-pulse response extracted from (b). (d) Schematic illustration of the optical communication system employing the AgNWs@p-ZnO:Sb MW/i-MgO/n-ZnO detector as the signal receiver. (e) Waveforms of the digitally encoded data captured by the PD.

AgNWs, are further discussed in Fig. S8. By comparison, the developed effective interface optimization by combining a MgO nanolayer and surface-modified AgNWs can be employed to enhance the photocarrier transport. Therefore, this work presents a fascinating self-driving photodetection device in terms of UV light sensitivity. For comparison, Table 2 compares the figures of merit of our photodetection devices with those of other reported ZnO-based self-powered PDs. It is worth noting that the as-fabricated AgNWs@p-ZnO:Sb MW/i-MgO/n-ZnO detector displays comparable response characteristics. In particular, the response time and EQE are superior to those of most PDs. The fast response time is ascribed to the surface-modified AgNWs. That is, AgNWs as the transition layer facilitate the facile transport of photogenerated electron-hole pairs, leading to improved carrier mobility and transport performance of an individual ZnO:Sb MW. This effect results in a significant enhancement in charge carrier extraction speed and efficiency, thus strengthening the conversion efficiency of incident light to photocarriers [4]. Fig. S9 plots the transient current *I-t* characteristics of the AgNWs@p-ZnO:Sb MW/i-MgO/n-ZnO detector under 365-nm illumination at frequencies of 1, 10, and 100 Hz, displaying a consistent and rapid response to pulsed optical signals. In addition, the device can work well after 240 cycles of operation while still maintaining its initial UV response properties even after storage in air for 100 days (Fig. S10).

The achievement of a self-biased photodetecting device in UV wavelengths is receiving great attention due to its promising application in optical communication. Taking advantage of the

robust photoresponse performance, the AgNWs@p-ZnO:Sb MW/i-MgO/n-ZnO photodiode was combined with an optical communication system as a signal receiver, as shown in Fig. 5d. The desired information "NUAA" was input into the computer, which then translated it into the corresponding ASCII code "01001110010101010100000101000001" which was then transmitted to a signal generator, where "0" and "1" denote low and high voltages, respectively, thus effectively modulating the connected UV light source. This modulation allows the UV light source to emit light at a specific frequency. The related photodiode that acts as the signal receiver was positioned to intercept the modulated light, which prompted rapid signal detection within the detector. These detected changes were promptly recorded by the connected oscilloscope. The transmission results of the information through the device are depicted in Fig. 5e, where "01001110", "01010101", "01000001", and "01000001" refer to "N", "U", "A", and "A", respectively. It is clear that the detected signals exhibit remarkably high discernibility. Also, the waveforms obtained from the detection process perfectly match those of the initial information. These findings exhibit the exceptional precision and speed of information transmission realized by the photodiode. Hence, the AgNWs@p-ZnO:Sb MW/i-MgO/n-ZnO PD has great potential for optical communication applications [41].

A PD array composed of 81 detector elements (nine rows and nine columns) with identical device structures was fabricated on a ZnO substrate by using the aforementioned device fabrication process. A schematic of the detection system is illustrated in

Table 2 Comparison of performance indexes of self-powered ZnO-based PDs

PD	Wavelength	R (mA W^{-1})	D^* (Jones)	Response time	EQE (%)	Ref.
p-ZnO:Ag/n-ZnO nanofibers	360 nm	1.0	–	3.9 s/4.7 s	0.3	[21]
ZnO MWs/PANI	350 nm	0.6	–	0.11 ms/1.45 ms	0.2	[47]
ZnO/graphite	330 nm	9.5	4.3×10^8	2.0 s/3.2 s	3.6	[48]
ZnO/CsPbBr$_3$/GaN:Mg	365 nm	44.5	2.0×10^{12}	160 ms/150 ms	15.1	[49]
CQDs-ZnO NRs/PEDOT	365 nm	22.6	5.8×10^{11}	90 ms/120 ms	7.7	[50]
ZnO/GaN	350 nm	95.8	2.9×10^{12}	731.6 ms/53.1 ms	33.9	[24]
ZnO/Ga$_2$O$_3$ core-shell	251 nm	9.7	6.3×10^{12}	100 μs/900 μs	4.8	[51]
ZnO/CsPbBr$_3$/γ-CuI	465 nm	140.0	8.1×10^{13}	3.9 μs/1.8 μs	37.4	[45]
ZnO:Ga NRs/MAPbI$_3$/MoO$_3$	490 nm	340.0	1.3×10^{12}	2 ms/2 ms	86.0	[52]
p-ZnO:Sb MW/n-ZnO	365 nm	53.5	7.0×10^{12}	126.5 μs/3.7 ms	18.2	This work
p-ZnO:Sb MW/i-MgO/n-ZnO	365 nm	268.3	2.0×10^{13}	35.5 μs/1.5 ms	91.2	This work
AgNWs@p-ZnO:Sb MW/ i-MgO/n-ZnO	365 nm	292.2	6.9×10^{13}	16.4 μs/465.1 μs	99.3	This work
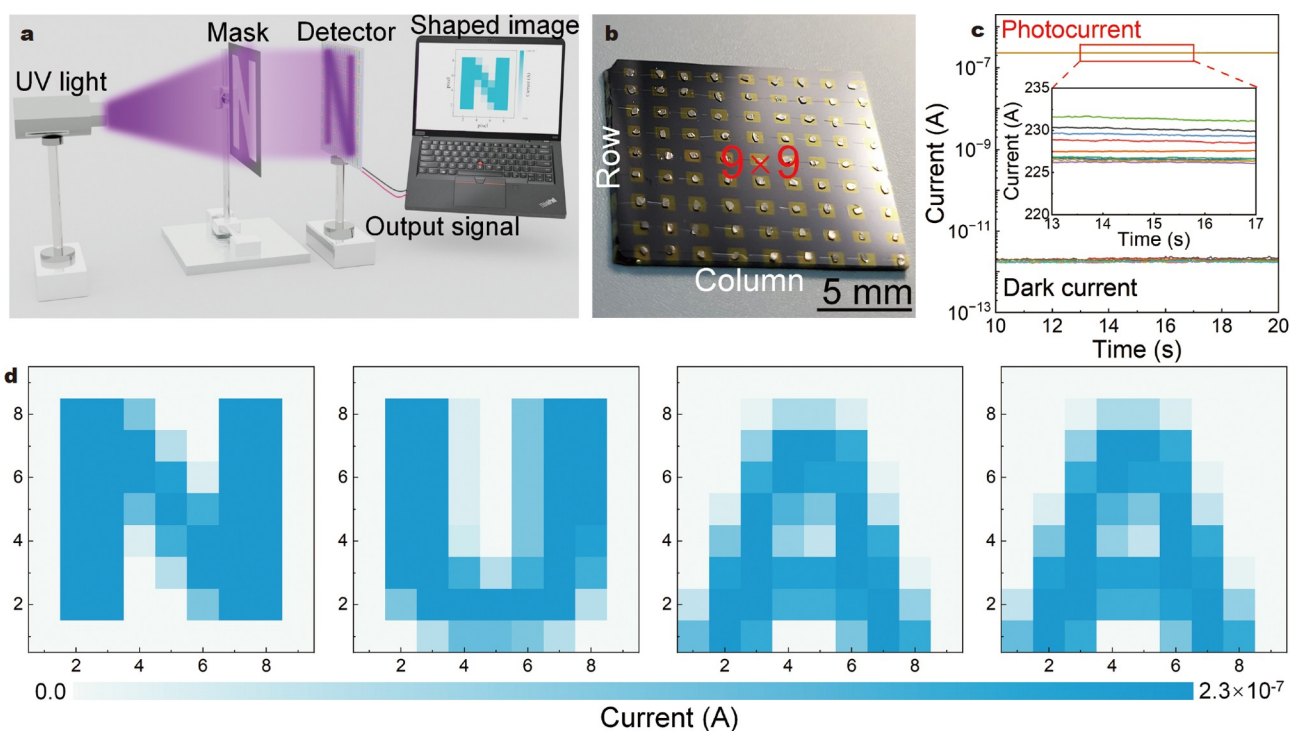
Figure 6 UV imaging sensor based on the PD array. (a) Schematic of the imaging system using the PD array as the sensing unit. (b) Photograph of the PD array. (c) Statistical *I-t* curves of devices in the 5th row of the array under 365-nm UV illumination and nonillumination conditions at 0 V bias. The inset shows *I-t* curves with an amplified current axis. (d) Corresponding images were acquired from the PD array with optical patterns of "N", "U", "A", and "A".

Fig. 6a [5,53]. Initially, a beam of UV light passes through the lens, transforming into a collimated beam. The collimated light is then vertically incident onto the surface of the mask. Then, a detector array matching the size of the mask is used to capture the UV light that passes through the apertures. On the surface of the PD array, the portion of detector units that are exposed to UV radiation can generate a distinguishable photocurrent. Thus, the variation in brightness resulting from the mask ultimately leads to the generation of the image. A photograph of the array device is presented in Fig. 6b. Considering the influence of factors such as the thickness of the ZnO film and MgO buffer

layer on device performance during the fabrication process, a series of detector units were subjected to *I-t* testing. Fig. 6c exhibits the *I-t* curves of the nine detectors unit (the 5th row) under illuminated and dark conditions at 0 V bias. Clearly, the photocurrent and dark current of each detector show outstanding stability, demonstrating no significant fluctuations over time. Only a slight numerical difference can be found from the magnified portion of the photocurrent (the inset of Fig. 6c). The average values of photocurrent and dark current are 2.28×10^{-7} and 1.86×10^{-12} A, with the corresponding coefficients of variation of 0.76% and 10.00%, respectively. These results pre-

liminarily demonstrate the high uniformity of the integrated device. Replacing different masks in front of the PD array, the imaging results are presented in Fig. 6d. All patterns are clearly identified from the imaging results, showing the potential utility of PD arrays for future UV imaging applications.

CONCLUSIONS

In this work, a high-performance self-powered UV photodiode based on the AgNWs@p-ZnO:Sb MW/i-MgO/n-ZnO homojunction was achieved. It demonstrates highly competitive figure-of-merit parameters, i.e., a maximum responsivity of 292.2 mA W^{-1}, the largest specific detectivity of 6.9×10^{13} Jones, and a rapid temporal response of 16.4 μs/465.1 μs at 0 V bias under 365-nm light illumination *via* 10 μW cm^{-2}. Particularly, the developed device has the largest EQE of approximately 99.3%, which is close to the theoretical limit. These unparalleled advantages are ascribed to the simultaneous introduction of the MgO interlayer and surface-modified AgNWs. The surface-modified AgNWs can compensate for the shortcomings of the MgO in-between buffer layer. They complement each other well, and the synergy provides an alternative interfacial engineering to obtain highly photosensitive PDs. This work gives a straight-forward and efficient approach to improving the performance of self-powered photodiodes, catering to their applications in the Internet of Things and fast photosensing fields.

1 Liu P, Yin L, Feng L, *et al.* Controllable preparation of ultrathin 2D BiOBr crystals for high-performance ultraviolet photodetector. Sci China Mater, 2021, 64: 189–197

2 Ouyang W, Chen J, Shi Z, *et al.* Self-powered UV photodetectors based on ZnO nanomaterials. Appl Phys Rev, 2021, 8: 031315

3 Wang Y, Chen C, Tang Z, *et al.* Tunable bandgap of black phosphorus by arsenic substitution toward high-performance photodetector. Sci China Mater, 2023, 66: 2364–2371

4 Wu D, Guo J, Du J, *et al.* Highly polarization-sensitive, broadband, self-powered photodetector based on graphene/PdSe$_2$/germanium heterojunction. ACS Nano, 2019, 13: 9907–9917

5 Li C, Wang H, Wang F, *et al.* Ultrafast and broadband photodetectors based on a perovskite/organic bulk heterojunction for large-dynamic-range imaging. Light Sci Appl, 2020, 9: 31

6 Song W, Chen J, Li Z, *et al.* Self-powered MXene/GaN van der Waals heterojunction ultraviolet photodiodes with superhigh efficiency and stable current outputs. Adv Mater, 2021, 33: 2101059

7 Du X, Tian W, Pan J, *et al.* Piezo-phototronic effect promoted carrier separation in coaxial p-n junctions for self-powered photodetector. Nano Energy, 2022, 92: 106694

8 Liu Y, Ji Z, Cen G, *et al.* Perovskite-based color camera inspired by human visual cells. Light Sci Appl, 2023, 12: 43

9 Wang M, Liang D, Ma W, *et al.* Significant performance enhancement of UV-vis self-powered CsPbBr$_3$ quantum dot-based photodetectors induced by ligand modification and P3HT embedding. Opt Lett, 2022, 47: 4512–4515

10 Li D, Zhou D, Xu W, *et al.* Plasmonic photonic crystals induced two-order fluorescence enhancement of blue perovskite nanocrystals and its application for high-performance flexible ultraviolet photodetectors. Adv Funct Mater, 2018, 28: 1804429

11 Li D, Xu W, Zhou D, *et al.* Cerium-doped perovskite nanocrystals for extremely high-performance deep-ultraviolet photoelectric detection. Adv Opt Mater, 2021, 9: 2100423

12 Ding N, Shao L, Xie T, *et al.* Highly-sensitive, stable, and fast-response lead-free Cs$_2$AgBiBr$_6$ double perovskite photodetectors enabled by synergistic engineering of doping Na$^+$/Ce^{3+} and integrating Ag nanoparticles film. Laser Photon Rev, 2022, 16: 2200301

13 Xu Z, Han X, Wu W, *et al.* Controlled on-chip fabrication of large-scale perovskite single crystal arrays for high-performance laser and photodetector integration. Light Sci Appl, 2023, 12: 67

14 Lin C, Wan P, Yang B, *et al.* Plasmon-enhanced photoresponse and stability of a CsPbBr$_3$ microwire/GaN heterojunction photodetector with surface-modified Ag nanoparticles. J Mater Chem C, 2023, 11: 12968–12980

15 Li Q, Huang J, Meng J, *et al.* Enhanced performance of a self-powered ZnO photodetector by coupling LSPR-inspired pyro-phototronic effect and piezo-phototronic effect. Adv Opt Mater, 2022, 10: 2102468

16 Qian L, Li W, Gu Z, *et al.* Ultra-sensitive β-Ga$_2$O$_3$ solar-blind photodetector with high-density Al@Al$_2$O$_3$ core-shell nanoplasmonic array. Adv Opt Mater, 2022, 10: 2102055

17 Li Z, Yu X, Zhu Y, *et al.* High performance ZnO quantum dot (QD)/magnetron sputtered ZnO homojunction ultraviolet photodetectors. Appl Surf Sci, 2022, 582: 152352

18 Wang Y, Wang P, Zhu Y, *et al.* High performance charge-transfer induced homojunction photodetector based on ultrathin ZnO nanosheet. Appl Phys Lett, 2019, 114: 011103

19 Tang K, Jiang M, Yang B, *et al.* Enhancing UV photodetection performance of an individual ZnO microwire p-n homojunction *via* interfacial engineering. Nanoscale, 2023, 15: 2292–2304

20 Tsai CH, Lin KC, Cheng CY, *et al.* GeSn lateral p-i-n waveguide photodetectors for mid-infrared integrated photonics. Opt Lett, 2021, 46: 864–867

21 Ning Y, Zhang Z, Teng F, *et al.* Novel transparent and self-powered UV photodetector based on crossed ZnO nanofiber array homojunction. Small, 2018, 14: 1703754

22 Wang Q, Zou A, Yang L, *et al.* Wide-bandgap semiconductor microtubular homojunction photodiode for high-performance UV detection. J Alloys Compd, 2021, 887: 161429

23 Su L, Zhao L, Chen SY, *et al.* Schottky-type GaN-based UV photodetector with atomic-layer-deposited TiN thin film as electrodes. Opt Lett, 2022, 47: 429–432

24 Mishra M, Gundimeda A, Garg T, *et al.* ZnO/GaN heterojunction based self-powered photodetectors: Influence of interfacial states on UV sensing. Appl Surf Sci, 2019, 478: 1081–1089

25 Chen Z, Li B, Mo X, *et al.* Self-powered narrowband p-NiO/n-ZnO nanowire ultraviolet photodetector with interface modification of Al$_2$O$_3$. Appl Phys Lett, 2017, 110: 123504

26 Liu M, Jiang M, Zhao Q, *et al.* Ultraviolet exciton-polariton light-emitting diode in a ZnO microwire homojunction. ACS Appl Mater Interfaces, 2023, 15: 13258–13269

27 Dehzangi A, Li J, Razeghi M. Band-structure-engineered high-gain LWIR photodetector based on a type-II superlattice. Light Sci Appl, 2021, 10: 17

28 Wu D, Guo J, Wang C, *et al.* Ultrabroadband and high-detectivity photodetector based on WS$_2$/Ge heterojunction through defect engineering and interface passivation. ACS Nano, 2021, 15: 10119–10129

29 Chen P, Atallah TL, Lin Z, *et al.* Approaching the intrinsic exciton physics limit in two-dimensional semiconductor diodes. Nature, 2021, 599: 404–410

30 Cai Q, You H, Guo H, *et al.* Progress on AlGaN-based solar-blind ultraviolet photodetectors and focal plane arrays. Light Sci Appl, 2021, 10: 94

31 Wang H, Wang W, Zhong Y, *et al.* Approaching the external quantum efficiency limit in 2D photovoltaic devices. Adv Mater, 2022, 34: 2206122

32 Wu F, Li Q, Wang P, *et al.* High efficiency and fast van der Waals hetero-photodiodes with a unilateral depletion region. Nat Commun, 2019, 10: 4663

33 Ripain AHA, Zulkifli NAA, Tan CL, *et al.* Highly efficient and stable near-infrared photo sensor based on multilayer MoS$_2$/p-Si integrated with plasmonic gold nanoparticles. Appl Phys Lett, 2023, 123: 061104

34 Zhu X, Xu J, Qin F, *et al.* Highly efficient and stable transparent electromagnetic interference shielding films based on silver nanowires. Nanoscale, 2020, 12: 14589–14597

35 Zhang J, Wang Y, Li D, *et al.* Engineering surface plasmons in metal/nonmetal structures for highly desirable plasmonic photodetectors.

ACS Mater Lett, 2022, 4: 343–355

36 Wan P, Jiang M, Xu T, *et al.* High-mobility induced high-performance self-powered ultraviolet photodetector based on single ZnO microwire/PEDOT:PSS heterojunction *via* slight Ga-doping. J Mater Sci Tech, 2021, 93: 33–40

37 Liu W, Xiu F, Sun K, *et al.* Na-doped p-type ZnO microwires. J Am Chem Soc, 2010, 132: 2498–2499

38 Wang G, Chu S, Zhan N, *et al.* ZnO homojunction photodiodes based on Sb-doped p-type nanowire array and n-type film for ultraviolet detection. Appl Phys Lett, 2011, 98: 041107

39 Wang CX, Yang GW, Liu HW, *et al.* Experimental analysis and theoretical model for anomalously high ideality factors in ZnO/diamond p-n junction diode. Appl Phys Lett, 2004, 84: 2427–2429

40 Peng Y, Lu J, Wang X, *et al.* Self-powered high-performance flexible GaN/ZnO heterostructure flexible UV photodetectors with piezo-phototronic effect enhanced photoresponse. Nano Energy, 2022, 94: 106945

41 Fang S, Li L, Wang D, *et al.* Breaking the responsivity-bandwidth trade-off limit in GaN photoelectrodes for high-response and fast-speed optical communication application. Adv Funct Mater, 2023, 33: 2214408

42 Wang L, Jie J, Shao Z, *et al.* MoS$_2$/Si heterojunction with vertically standing layered structure for ultrafast, high-detectivity, self-driven visible-near infrared photodetectors. Adv Funct Mater, 2015, 25: 2910–2919

43 Shui ZD, Wang S, Yang Z, *et al.* Polarization-sensitive self-powered tellurium microwire near-infrared photodetector. Appl Phys Lett, 2023, 122: 101902

44 Xian S, Hou S, Zhang H, *et al.* High quality quasi-two-dimensional organic–inorganic hybrid halide perovskite film for high performance photodetector. Appl Phys Lett, 2023, 122: 103510

45 Xing R, Shi P, Wang D, *et al.* Flexible self-powered weak light detectors based on ZnO/CsPbBr$_3$/γ-CuI heterojunctions. ACS Appl Mater Interfaces, 2022, 14: 40093–40101

46 Zhang Q, Li N, Zhang T, *et al.* Enhanced gain and detectivity of unipolar barrier solar blind avalanche photodetector *via* lattice and band engineering. Nat Commun, 2023, 14: 418

47 Chen Y, Su L, Jiang M, *et al.* Switch type PANI/ZnO core-shell microwire heterojunction for UV photodetection. J Mater Sci Tech, 2022, 105: 259–265

48 Sinha R, Roy N, Mandal TK. Growth of carbon dot-decorated ZnO nanorods on a graphite-coated paper substrate to fabricate a flexible and self-powered Schottky diode for UV detection. ACS Appl Mater Interfaces, 2020, 12: 33428–33438

49 Huang Y, Zhang L, Wang J, *et al.* Enhanced photoresponse of n-ZnO/p-GaN heterojunction ultraviolet photodetector with high-quality CsPbBr$_3$ films grown by pulse laser deposition. J Alloys Compd, 2019, 802: 70–75

50 Serkjan N, Liu X, Abdiryim T, *et al.* Organic-inorganic face-to-face ZnO NRs-based self-powered UV photodetectors: Heterojunction with poly(3,4-ethylenedioxyselenophene) and enhanced responsivity by carbon quantum dots. Carbon, 2023, 204: 387–397

51 Zhao B, Wang F, Chen H, *et al.* An ultrahigh responsivity (9.7 mA W^{-1}) self-powered solar-blind photodetector based on individual ZnO-Ga$_2$O$_3$ heterostructures. Adv Funct Mater, 2017, 27: 1700264

52 Zhou H, Yang L, Gui P, *et al.* Ga-doped ZnO nanorod scaffold for high-performance, hole-transport-layer-free, self-powered CH$_3$NH$_3$PbI$_3$ perovskite photodetectors. Sol Energy Mater Sol Cells, 2019, 193: 246–252

53 Deng M, Li Z, Deng X, *et al.* Wafer-scale heterogeneous integration of self-powered lead-free metal halide UV photodetectors with ultrahigh stability and homogeneity. J Mater Sci Tech, 2023, 164: 150–159

Author contributions Jiang M and Shi D supervised the project and the experiments. Tang K performed the experiments with the assistance of Sha S, Zhai Y and Wan P. Tang K wrote the paper with support from Jiang M and Kan C. The other authors helped analyze the results, contributed to the theoretical analysis and revised this paper. All authors contributed to the general discussion.

Conflict of interest The authors declare that they have no conflict of interest.

Supplementary information Experimental details and supporting data are available in the online version of the paper.

Kai Tang received his BS degree in physics from Anyang Normal University, Henan, in 2019. Currently, he is pursuing his PhD degree at the College of Physics, Nanjing University of Aeronautics and Astronautics, Nanjing, China. His current research interests focus on ZnO-based homojunction ultraviolet detectors.

Mingming Jiang received his BS degree from Dalian University of Technology, Dalian, China, and his PhD degree from the University of Science and Technology of China (USTC), Hefei, China. He was an associate professor at Changchun Institute of Optics, Fine Mechanics and Physics, Chinese Academy of Sciences, Changchun, China. He is currently a full professor at the College of Physics, Nanjing University of Aeronautics and Astronautics, Nanjing, China. His current research interest is low-dimension wide bandgap semiconductor optoelectronics.

Daning Shi received his BS degree from Suzhou University in 1984 and his PhD degree from Nanjing University in 1999. He is currently a professor and vice president of Nanjing University of Aeronautics and Astronautics. His main research interests are condensed matter theory and computational nanophysics.

界面工程与等离激元效应协同作用增强的ZnO微米线同质结自驱动紫外探测器

唐楷，沙树林，万鹏，翟亚林，阚彩侠，施大宁*，姜明明*

摘要 高灵敏度的自驱动紫外探测器在许多应用中都大有可为. 本研究提出了一种一维ZnO基同质结光电探测器，它包括表面覆盖着Ag纳米线的锑掺杂ZnO微米线(AgNWs@ZnO:Sb MW)、MgO缓冲纳米层和ZnO薄膜. 该探测器在0 V偏压下对紫外光非常敏感，其性能参数包括约7个量级的开关比、292.2 mA W^{-1}的响应度、6.9 × 10^{13} Jones的比探测率，以及微秒量级的快速响应速度(上升时间16.4 μs，下降时间465.1 μs). 特别是10 μW cm^{-2}的微弱紫外光时接近99.3%的外量子效率. 此外，本文系统研究了MgO纳米薄膜和表面修饰AgNWs对探测器件性能增强的机理. 作为自驱动光接收器，该光电二极管被进一步集成到能够实时传输信息的紫外通信系统中. 此外，基于AgNWs@p-ZnO:Sb MW/i-MgO/n-ZnO的同质结9 × 9阵列显示出均匀的光响应分布，可用作具有良好空间分辨率的成像传感器. 这项研究有望为设计高性能紫外光检测器提供一条具有低功耗和可大规模建造的途径.